Euler–Lagrange/DEM simulation of wood gasification in a bubbling fluidized bed reactor

Michael Oevermann*, Stephan Gerber, Frank Behrendt

Berlin Institute of Technology, School of Process Sciences and Engineering, Department of Energy Engineering, Fasanenstr. 89, 10623 Berlin, Germany

ABSTRACT

We present an Euler–Lagrange method for the simulation of wood gasification in a bubbling fluidized bed. The gas phase is modeled as a continuum using the 2D Navier–Stokes equations and the solid phase is modeled by a Discrete Element Method (DEM) using a soft-sphere approach for the particle collision dynamic. Turbulence is included via a Large-Eddy approach using the Smagorinsky sub-grid model. The model takes into account detailed gas phase chemistry, zero-dimensional modeling of the pyrolysis and gasification of each individual particle, particle shrinkage, and heat and mass transfer between the gas phase and the particulate phase. We investigate the influence of wood feeding rate and compare exhaust gas compositions and temperature results obtained with the model against experimental data of a laboratory scale bubbling fluidized bed reactor.

© 2009 Chinese Society of Particuology and Institute of Process Engineering, Chinese Academy of Sciences. Published by Elsevier B.V. All rights reserved.

1. Introduction

Wood gasification is a very old technique dating back to the beginnings of the industrial revolution. The recent discussions on climate change, CO_2 emissions, and the limited availability of fossil fuels have renewed the interest in gas from biomass and wood. Current biomass gasification systems comprise fixed and moving bed reactors, fluidized or circulating fluidized bed reactors, and pulverized fuel burners. Advantages of fluidized bed reactors are, e.g., the good heat and mass transfer between the gas phase and the individual particles and a good performance for a wide range of fuel qualities. Despite the long tradition of utilizing the combustible fuel gas from wood gasification, there still is a lack of detailed scientific knowledge about the complex interactions between the gasification reactions and the fluid mechanics of fluidized beds.

In order to improve and optimize the thermal efficiency and to predict product gas composition and emission rates, numerous mathematical models for coal – and more recently biomass – gasification in fluidized beds have been developed. The modeling approaches are ranging from simple equilibrium models (e.g., Li et al., 2004), zone/cell models (e.g., Jennen, Hiller, Köneke,

& Weinspach, 1999; Hamel & Krumm, 2001; Gungor, 2008), one-dimensional models (Radmanesh, Chaouki, & Guy, 2006), to sophisticated Euler–Lagrange models combined with large-Eddy modeling of the turbulent gas phase (Zhou, Flamant, & Gauthier, 2004a, 2004b). Whereas the simpler models such as zone/cell models and equilibrium models are suitable for design optimization of industrial size gasifiers, the more comprehensive models as Euler–Euler (Lathouwers & Bellan, 2001a; Agrawal, Loezos, Syamlal, & Sundaresan, 2001; O'Brien, Syamlal, & Guenther, 2003) and Euler–Lagrange (Rong & Horio, 1999; Kaneko, Shiojima, & Horio, 1999; Zhou et al., 2004a, 2004b; Limtrakul, Boonsrirat & Vatanatham, 2004) models are more targeted towards fundamental investigations of the chemical and fluid mechanical aspects of fluidized beds.

In the Euler–Euler modeling approach the particulate phase is considered as a continuous phase interpenetrating and interacting with the gas phase. Polydisperse systems can be modeled with this approach via multiple solid phases where each phase characterizes a different particle class. The kinetic theory of granular flow (Ding & Gidaspow, 1990; Gidaspow, 1994) is used as a theoretical framework to derive constitutive equations for the solid phases and the gas–particle interactions. Euler–Euler models allow a relatively realistic description of the time dependent processes in non-reacting (Agrawal et al., 2001) and reacting fluidized beds (Lathouwers & Bellan, 2001a, 2001b). However, one of

---

* Corresponding author. Tel.: +49 30 314 22452; fax: +49 30 314 22157.
E-mail address: michael.oevermann@tu-berlin.de (M. Oevermann).

Nomenclature

A	pre-exponential factor, 1/s or particle surface area (m^2)
c_p	specific heat at constant pressure (J/(kg K))
C_D	drag coefficient (dimensionless)
C_R	torque coefficient (dimensionless)
d_P	particle diameter (m)
e	mass-specific internal energy (J/kg)
Ea	activation energy (kJ/mole)
$\boldsymbol{F}$	force (N)
$\boldsymbol{F}_i$	total force acting on particle i (N)
$\boldsymbol{F}_s$	momentum exchange term (N/m^3)
g	gravitational acceleration (m/s^2)
I	unit tensor
k_n, k_t	stiffness coefficients (N/m)
m_{cc}	charcoal mass (kg)
m_p	particle mass (kg)
m_w	wood mass (kg)
$\boldsymbol{n}$	unit normal vector (dimensionless)
p	pressure (Pa)
$\boldsymbol{q}$	heat flux vector (W/m^2)
$\dot{Q}_s$	heat transfer term (W/m^3)
$\dot{r}_\alpha$	reaction rate for component α (1/s)
R_α	individual gas-constant of species α (J/(kg K))
Re_p	particle Reynolds number
t	time (s)
$\boldsymbol{t}$	unit tangential vector (dimensionless)
T	particle temperature (K)
$\boldsymbol{T}_C$	torque due to collisions (N m)
$\boldsymbol{T}_F$	torque due to friction (N m)
T_g	gas phase temperature (K)
$\boldsymbol{T}_i$	total torque acting on particle i (N m)
$\boldsymbol{u}_g$	gas phase velocity (m/s)
v	particle velocity (m/s)
V	volume of a computational cell (m^3)
V_p	particle volume (m^3)
$\dot{w}_{\alpha,g}$	gas phase chemical source term (kg/(m^3 s))
$\dot{w}_{\alpha,s}$	solid phase source term (kg/(m^3 s))
X_α	mole-fraction of species α (dimensionless)
Y_α	mass-fraction of species α (dimensionless)

Greek letters

α	heat transfer coefficient (W/(m^2 K))
Δh_α^0	heat of formation (J/kg)
ε	void fraction, dimensionless or emissivity (dimensionless)
η	interpolation factor (dimensionless)
η_n, η_t	damping coefficients (N/(m s))
μ_f	friction coefficient (dimensionless)
μ_g	gas phase bulk viscosity (kg/(m s))
ρ_g	gas phase density (kg/m^3)
ρ_p	particle bulk density (kg/m^3)
σ	Stefan–Boltzmann constant (J/K)
τ	gas phase stress tensor (Pa)
$\boldsymbol{\omega}$	angular velocity vector (1/s)
$\boldsymbol{\Omega}$	relative angular velocity vector (1/s)

Subscripts

C	collision
cc	charcoal
g	gas phase
i, j	particle index
n	time level or normal direction
p	particle
t	tangential direction
w	solid wood
wg	wood gas

the most severe difficulties associated with Euler–Euler models are the complicated closure models describing the mass, momentum, and energy transfer between multiple continuous phases, which are usually not universally valid.

In Euler–Lagrange models the trajectory and the state (temperature, mass, composition, and velocity) of each individual particle are tracked in space and time by integrating the equations of motion, energy, and mass for each particle in the system. For dense particle system with multiple contacts between particles the soft-sphere model or discrete/distinct element method (DEM) is usually applied. Since the pioneering work of Cundall and Strack (1979), this type of models has been used for a wide range of applications involving particles. Tsuji, Kawaguchi and Tanaka (1993) are usually cited as the first authors who coupled the Navier–Stokes equations with a soft-sphere model. In soft-sphere models the contact forces are calculated from the deformation history using a contact force model. The simplest one, which is also used in this work, goes back to the original work of Cundall and Strack (1979) and models the contact force between particles by employing a linear spring and a dash pot. A review of discrete particle modeling of fluidized beds can be found in the recent publications of Deen, van Sint Annaland, van der Hoef and Kuipers (2007) and Tsuji (2000).

From all the above mentioned models the Euler–Lagrange approach potentially offers the most accurate description not only of the particle motion (translational and rotational, particle–particle collisions) but also of chemical reactions and heat and mass transfer between the dispersed phase and the gas phase at the individual particle scale. Although one can find quite many publications of inert particle simulations using the DEM, only few applications of the DEM for particle systems involving heat and mass transfer and chemical reactions are available in the literature. As an example, Kaneko et al. (1999) used the DEM approach for the simulation of olefin polymerization in a fluidized bed. A comparable model has been applied by Limtrakul et al. (2004) for the modeling of the local mass transfer in a catalytic gas–solid fluidized bed reactor. Another example of using the DEM approach for the numerical investigation of heat transfer in hoppers was presented by Kruggel-Emden, Wirtz, Simsek and Scherer (2006). Zhou et al. (2004a) formally coupled a large eddy turbulence model with a discrete element method and applied their method for the simulation of coal combustion (Zhou et al., 2004b). However, in their 2D simulations they used only 20 reactive coal and 2000 inert sand particles in their simulation of a bubbling fluidized bed and the presented simulation results correspond to only 2 s of real time. In some recent publications of Papadikis, Bridgwater and Gu (2008), and Papadikis, Gu, and Bridgwater (2009a, 2009b) two- and three-dimensional calculations of biomass pyrolysis using discrete particles are presented. Only two discrete and reactive particles have been included in the simulations and the inert sand particles are modeled as a continuum. Furthermore, a very small reactor of 40 mm diameter and 260 mm height was considered and no comparison with experimental data was provided in any of the three papers. The presented simulation times in Papadikis et al. (2008, 2009a,b) are 3–4 s of real time.

In this work we present an Euler–Lagrange/DEM modeling approach for the simulation of wood gasification in a bubbling

fluidized bed. The long-term aim is the development of a simulation tool which allows a realistic and detailed modeling of the complex interactions between the fluid mechanics, chemistry, heat and mass transfer in dense particulate flow at the particle scale. Here we present a first description of the model with an application to the simulation of wood gasification in a bubbling fluidized bed. We put the emphasis of the investigation on the influence of chemical reactions on the fluidization. Euler–Lagrange/DEM simulations with a soft-sphere collision model are computationally very demanding. This is all the more true if – as in this study – chemically reacting particle flows are considered. Although the presented method is implemented fully three-dimensionally, we restrict the investigations here to a two-dimensional setting. This restriction limits somehow the realistic description of the inherently three-dimensional character of polydisperse particulate flow, but it allows us to present representative computational results for simulation times up to 100 s of real time. We consider detailed models for the pyrolysis, heterogeneous gasification reactions, and homogeneous gas phase chemistry. We present results for different wood feeding rates and compare results of the temperature and exhaust gas composition with experimental data of a laboratory scale fluidized bed reactor.

2. Mathematical modeling

2.1. Continuous phase

The gas phase is modeled as a continuum, which can be described by a set of volume averaged Navier–Stokes equation (Kuo, 1986). Turbulence is modeled with a Large-Eddy simulation (LES) approach, where the flow variables are decomposed into a resolved component and an unresolved sub-grid scale component. In accordance with Zhou et al. (2004a) we neglect explicit sub-grid scale modeling in the energy and mass balance equations.

For the global mass balance we have in conservative form:

$$\frac{\partial \varepsilon \rho_g}{\partial t} + \nabla(\varepsilon \rho_g \boldsymbol{u}_g) = 0, \tag{1}$$

where ε, ρ_g, and $\boldsymbol{u}_g$ are the void fraction, the gas density, and the gas phase velocity, respectively. The balance equations for the individual species α in the gas phase can we written as:

$$\frac{\partial \varepsilon \rho_g Y_\alpha}{\partial t} + \nabla(\varepsilon \rho_g Y_\alpha \boldsymbol{u}_g) = \varepsilon \dot{w}_{\alpha,g} + \varepsilon \dot{w}_{\alpha,s}. \tag{2}$$

Here Y_α denotes the mass-fraction of species α in the gas phase, $\dot{w}_{\alpha,g}$ is the net production rate of species α due to gas phase chemical reactions, and $\dot{w}_{\alpha,s}$ is the mass transfer term between the solid phase and the gas phase.

The filtered gas phase momentum equation is:

$$\frac{\partial \varepsilon \rho_g \boldsymbol{u}}{\partial t} + \nabla(\varepsilon \rho_g \boldsymbol{u}_g \boldsymbol{u}_g) + \varepsilon \nabla p + \varepsilon(\nabla \tau) + \varepsilon \rho_g \boldsymbol{g} = \boldsymbol{F}_s. \tag{3}$$

Here, p, τ, $\boldsymbol{g}$, and $\boldsymbol{F}_s$ are the pressure, the gas phase stress tensor, the gravitational force, and the momentum exchange term between the gas phase and the particulate phase, respectively. The gas phase stress tensor is modeled as:

$$\tau = -\mu_{\text{eff},g}\left(\nabla \boldsymbol{u}_g + \nabla \boldsymbol{u}_g^T - \frac{2}{3}\nabla \boldsymbol{u}_g I\right),$$

where $\mu_{\text{eff},g}$ is the effective viscosity which is based on the model of Smagorinsky (1963) and can be written as the sum of the laminar viscosity and a sub-grid scale viscosity representing the unresolved turbulent part of the velocity field:

$$\mu_{\text{eff},g} = \mu_{\text{lam}} + \mu_{\text{turb}} = \mu_{\text{lam}} + \rho_g(c_t \Delta)^2 \sqrt{\boldsymbol{S} : \boldsymbol{S}}$$

Table 1
Kinetic parameters for the primary pyrolysis according to Eq. (8).

Product P	A in 1/s	E_a in kJ/mole
Wood gas	1.43×10^4	88.6
Tar	4.13×10^6	112.7
Charcoal	7.38×10^5	106.5

The sub-grid scale eddy coefficient c_t is set to 0.079 (Deardoff, 1971), for the length scale we have $\Delta = (\Delta x \, \Delta y \, \Delta z)^{1/3}$, and the strain tensor of the resolved flow field is given by:

$$\boldsymbol{S} = \frac{1}{2}(\nabla u_g + \nabla u_g^T).$$

The balance equation for the mass-specific energy e can be written as:

$$\frac{\partial \varepsilon \rho_g e}{\partial t} + \nabla(\varepsilon u_g(\rho_g e + p)) + \varepsilon(\nabla \boldsymbol{q}) = \dot{Q}_s, \tag{4}$$

where $\boldsymbol{q}$ is the heat flux vector and $\dot{Q}_s$ denotes the heat transfer term between the solid phase and the gas phase. Here e is the sum of the internal energy plus the chemical energy. In the limit of a small or vanishing Mach-number Ma the kinetic energy and the contribution of the viscous stresses can be neglected in the total energy budget as they scale as Ma^2 (Klein, 1999; Klein et al., 2001).

The temperature is implicitly given by the caloric equation of state:

$$e(T) = \sum_\alpha Y_\alpha e_\alpha(T), \tag{5}$$

where $e_\alpha(T)$ is the mass-specific energy of species α which depends on temperature only for an ideal gas:

$$e_\alpha(T) = \Delta h_\alpha^0 + \int_{T^0}^{T} c_{p,\alpha}(T)\,dT,$$

where Δh_α^0 is the heat of formation at reference temperature T^0 and $c_{p,\alpha}(T)$ is the mass-specific heat capacity at constant pressure for species α. The pressure is given by the equation of state for an ideal gas as:

$$p = \rho_g T \sum_\alpha Y_\alpha R_\alpha, \tag{6}$$

where R_α is the individual gas-constant of species α.

The void fraction ε in each computational cell is calculated based on the actual number n of particles within that cell:
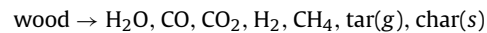
$$\varepsilon = 1 - \frac{1}{V}\sum_{i=1}^{n} V_i, \tag{7}$$

where V is the volume of the computational cell and V_i is the volume of particle i within the cell.

2.2. Disperse phase/discrete element model

2.2.1. Pyrolysis

Primary pyrolysis denotes the decomposition of solid biomass into wood gas, gaseous tar, and the solid compound char:

wood → H_2O, CO, CO_2, H_2, CH_4, tar(g), char(s)

The reaction rates for the products P in the form:

$$\dot{r}_P = A \exp\left(\frac{-E_a}{RT}\right), \quad [\text{s}^{-1}] \tag{8}$$

are taken from Gronli (1996) and are summarized in Table 1. Primary pyrolysis usually is followed by secondary cracking of tar into

Table 2
Fixed gas composition after pyrolysis.

No.	Component	Weight fraction
1	H_2	0.02444
2	H_2O	0.05842
3	CH_4	0.10036
4	CO	0.61891
5	CO_2	0.19787

gaseous compounds and inert tar. Here we adopt a simplified model and assume that the secondary pyrolysis is able to crack all tar from the primary pyrolysis and so actually no tar needs to be added to the gas phase. This seems to be justifiable insofar as there are some uncertainties about the existence of inert tar after the secondary cracking of tar (Wurzenberger, Wallner, Raupenstrauch, & Khinast, 2002). Investigations by Rath et al. (2003) show that the heat of wood pyrolysis is relatively small and that the amount of inert tar is small. Therefore, we assume a heat-neutral pyrolysis step in this work and neglect inert tar.

Table 2 shows the fixed composition of the gas from primary and secondary pyrolysis which is taken from the work of Wurzenberger et al. (2002).

However, we remark that tar is an important problem in the utilization of wood gas in subsequent steps like gas motors or gas turbines. A detailed investigation of different models for primary and secondary pyrolysis in the Euler–Lagrange model will be presented in a in press publication.

2.2.2. Heterogeneous reactions

Heterogeneous reactions of solid char with species in the gas phase are modeled using the following overall reactions:

$$
\begin{aligned}
&C + O_2 \rightarrow CO_2 \quad \text{(i)}\\
&C + CO_2 \rightarrow 2CO \quad \text{(ii)}\\
&C + H_2O \rightarrow CO + H_2 \quad \text{(iii)}
\end{aligned}
\tag{9}
$$

The rate expressions and kinetic parameters for (i), (ii), and (iii) are taken from Ross and Davidson (1982), Biggs and Agarwal (1997), and Hobbs, Radulovic and Smoot (1992), respectively, and are summarized in Table 3. In the rate expressions of Biggs and Agarwal (1997), (Eq. (9-ii)), one has to use the inner surface of the particle. Using the ratio of the inner surface area S_i to the volume V of the particle, $\xi = S_i/V = 3.2 \times 10^7 \, \text{m}^2/\text{m}^3$, we can transform the rate expression for CO_2 into a reaction rate per unit volume:

$$
\dot{r}_{CO_2} = \xi f(\varepsilon) \dot{\tilde{r}}_{CO_2}, \quad [\text{mol m}^{-3} \text{ s}^{-1}],
\tag{10}
$$

where $\dot{\tilde{r}}_{CO_2}$ is given in Table 3. Here we do not explicitly calculate the inner porosity of the particles and assume a constant value of 0.5. This leads according to Biggs and Agarwal (1997) to $f(\varepsilon) = 1.44$ in Eq. (10).

Table 3
Reaction rates and kinetic parameters for the heterogeneous reactions as shown in Eq. (9).

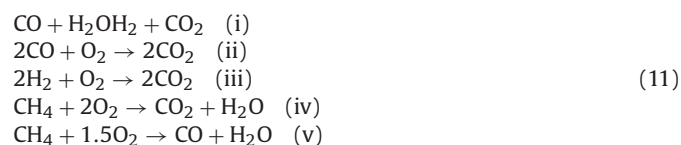| Heterogeneous rate expression	Unit
$\dot{r}_{O_2}^{(i)} = 1.5 \times 10^6 \, \exp\left(\frac{-13078}{T}\right) p_{O_2}(1 - X_c)^{1.2}$	1/s
$\dot{\tilde{r}}_{CO_2}^{(ii)} = 4364 \, \exp\left(\frac{-30178}{T}\right) c_{CO_2}$	mol/(s m^2)
$\dot{r}_{H_2O}^{(iii)} = \frac{k_1 p_{H_2O}}{1 + k_2 p_{H_2O} + k_3 p_{H_2}}$	1/s
$k_1 = 4.93 \times 10^3 \, \exp\left(\frac{-18522}{T}\right)$	1/(bar s)
$k_2 = 1.11 \times 10^1 \, \exp\left(\frac{-3548}{T}\right)$	1/bar
$k_3 = 1.53 \times 10^{-9} \, \exp\left(\frac{25161}{T}\right)$	1/bar

Table 4
Reaction rates and kinetic parameters for the homogeneous gas phase reactions as shown in Eq. (11).

Homogeneous rate expression	Unit
$\dot{r}_{CO}^{(i)} = 2.78 \times 10^3 \, \exp\left(\frac{-1510}{T}\right) c_{CO} c_{H_2O}$	mol/(m^3 s)
$\dot{r}_{CO_2}^{(ii)} = 3.98 \times 10^{14} \, \exp\left(\frac{-20119}{T}\right) c_{CO} c_{O_2}^{0.25} c_{H_2O}^{0.5}$	mol/(m^3 s)
$\dot{r}_{H_2}^{(iii)} = 2.19 \times 10^{12} \, \exp\left(\frac{-13127}{T}\right) c_{H_2} c_{O_2}$	mol/(m^3 s)
$\dot{r}_{CH_4}^{(iv)} = 1.58 \times 10^{13} \, \exp\left(\frac{-24343}{T}\right) c_{CH_4} c_{O_2}$	mol/(m^3 s)
$\dot{r}_{CH_4}^{(v)} = 1.58 \times 10^{13} \, \exp\left(\frac{-24155}{T}\right) c_{CH_4}^{0.7} c_{O_2}^{0.8}$	mol/(m^3 s)

2.3. Homogeneous gas phase reactions

In the present work the following simple kinetic mechanism for syngas has been used:

$$
\begin{aligned}
&CO + H_2O \rightleftharpoons H_2 + CO_2 \quad \text{(i)}\\
&2CO + O_2 \rightarrow 2CO_2 \quad \text{(ii)}\\
&2H_2 + O_2 \rightarrow 2CO_2 \quad \text{(iii)}\\
&CH_4 + 2O_2 \rightarrow CO_2 + H_2O \quad \text{(iv)}\\
&CH_4 + 1.5O_2 \rightarrow CO + H_2O \quad \text{(v)}
\end{aligned}
\tag{11}
$$

where the reaction rates and kinetic parameters for (i) are taken from De Souza-Santoz (1989), for (iii) from Mitani and Williams (1980), for (iv) from Dryer and Glassman (1972) and for reactions (ii) and (v) from Dryer (1972). Only the first reaction is modeled as an equilibrium reaction which favors the production of CO and H_2O at higher temperatures and CO_2 and H_2 at lower temperatures. The equilibrium of the last three equations is far on the product side under typical gasification conditions. For simplicity, reverse reactions were neglected here. The kinetic parameters for all reactions are from the cited literature and are summarized in Table 4.

2.3.1. Zero-dimensional particle model

For each particle in the system we solve a set of three ordinary differential equations to model pyrolysis, gasification, and shrinkage of the particle. The zero-dimensional model consists of equations for the wood mass m_w, the particle temperature T, and the charcoal mass m_{cc}:

$$
\begin{aligned}
&\frac{dm_w}{dt} = -(\dot{r}_{wg} + \dot{r}_{tar(g)} + \dot{r}_{cc})m_w,\\[6pt]
&c_p m_p \frac{dT}{dt} = \sum_i (\Delta h_i w_i) + \alpha A(T - T_g) + \varepsilon \sigma A(T^4 - T_g^4),\\[6pt]
&\frac{dm_{cc}}{dt} = -(\dot{r}_{H_2O} + \dot{r}_{CO})m_{cc} - V_p M_p \dot{r}_{CO_2},
\end{aligned}
\tag{12}
$$

where c_p is the mass-specific heat capacity of the particle, $m_p = m_w + m_{cc}$ is the total mass of the particle, Δh_i is the heat of reaction of the heterogeneous reaction i with reaction rate w_i, α is the heat transfer coefficient, A is the surface area of the particle, σ is the Stefan–Boltzmann constant, ε is the emissivity with an assumed value of 0.7, V_p is the volume of the particle, and M_p is the mean molar mass of the particle. The reaction rates for the conversion of wood (index w) into wood gas (index wg), tar (index t), and charcoal (index cc) in the first equation of Eq. (12) are given by Eq. (8) and Table 1. The reaction rates for the charcoal conversion are from Table 3.

To ensure the use of a smooth transition of material properties from wood to charcoal we use an interpolation factor similar to the work of Gronli (1996), which we assume to be mass based instead

of density based:

$$\eta = \frac{m_{\mathrm{w}}}{m_{\mathrm{w},0} + m_{\mathrm{cc}}}, \tag{13}$$

where $m_{\mathrm{w},0}$ is the initial (wood) mass of the particle. With this interpolation factor we define a property ϕ:

$$\phi(\eta) = \eta\phi_{\mathrm{w}} + (1 - \eta)\phi_{\mathrm{cc}},$$

with $\phi = \rho, c_{\mathrm{p}}$. For the specific heats of wood and charcoal we use the following expressions from Gronli (1996):

$$c_{\mathrm{p,w}} = 1.5 + 1.0 \times 10^{-3}\, T \left[\mathrm{kJ/(kg\,K)}\right],$$
$$c_{\mathrm{p,cc}} = 0.42 + 2.09 \times 10^{-3}T + 6.85 \times 10^{-7}T^2 \left[\mathrm{kJ/(kg\,K)}\right].$$

Di Blasi (1996) shows a fairly general way to calculate the shrinkage of the solid particles, which would introduce an additional equation for the particle volume. In our work the shrinkage is simply assumed to be mass-proportional, i.e.:

$$r = \left(\frac{3}{4}\frac{m_p}{\pi\rho_p}\right)^{1/3}.$$

2.3.2. Particle movement

The motion of each particle in the system is calculated by integrating Newton's equation of motion:

$$\dot{\boldsymbol{x}} = v, \qquad \dot{\boldsymbol{v}} = \frac{1}{m_{\mathrm{p}}}\sum_i F_i, \qquad \dot{\boldsymbol{\omega}} = \frac{1}{I_{\mathrm{p}}}\sum_i T_i, \tag{14}$$

where $\boldsymbol{x}, v, \boldsymbol{\omega}$ are the position, the velocity and the angular velocity of the particle. I_{p} is the moment of inertia for the spherical particle with $I_{\mathrm{p}} = (1/10)m_{\mathrm{p}}d_{\mathrm{p}}^2$. Under the various forces acting on a single particle in a gas flow (drag, weight, buoyancy, Saffmann, Magnus, etc.) we consider only the drag force $\boldsymbol{F}_{\mathrm{D}}$ and the weight force $\boldsymbol{F}_g$. According to an analysis of Sommerfeld (2000), these are the dominant forces under the conditions in this work. This is also confirmed by an investigation of the relative forces acting on particles in a spout fluidized bed by Zhong, Xiong, Yuan and Zhang (2006). In that work Zhong et al. (2006) showed that drag, contact, and gravitational forces are the dominant forces in dense fluidized beds and that Magnus and Saffmann forces contribute together at most 6% of the total force acting on a particle.

The sums of the forces and torques acting on a particle can now be written as:

$$\sum_i \boldsymbol{F}_i = \boldsymbol{F}_{\mathrm{D}} + \boldsymbol{F}_g + \boldsymbol{F}_{\mathrm{C}}, \qquad \sum_i \boldsymbol{T}_i = \boldsymbol{T}_{\mathrm{F}} + \boldsymbol{T}_{\mathrm{C}}, \tag{15}$$

where $\boldsymbol{F}_{\mathrm{C}}$ is the force from collisions with other particles and the walls of the reactor, and $\boldsymbol{T}_{\mathrm{F}}$ and $\boldsymbol{T}_{\mathrm{C}}$, denote the torques due to viscous friction and particle–particle contacts.

The drag force is modeled using the usual correlation:

$$F_{\mathrm{D}} = \frac{1}{8}\pi C_{\mathrm{d}} f(\varepsilon)\varepsilon^2 \rho_g \left|\boldsymbol{u}_g - \boldsymbol{v}\right| (\boldsymbol{u}_g - \boldsymbol{v}) \tag{16}$$

The drag coefficient C_{d} distinguishes between the Stokes and the transient regime on the one hand and the Newton regime on the other hand:

$$C_{\mathrm{D}} = \begin{cases} \dfrac{24}{Re_P}(1 + 0.15Re_P^{0.687}), & Re_P < 1000 \\ 0,44, & Re \geq 1000 \end{cases} \tag{17}$$

where the particle Reynolds number Re_{P} is defined as:

$$Re_{\mathrm{P}} = \frac{\varepsilon \left|\boldsymbol{u}_{\mathrm{F}} - \boldsymbol{v}\right| d_{\mathrm{P}}}{\mu_g} \tag{18}$$

In the literature one can find quite many relations for the term $f(\varepsilon)$ in Eq. (16), see, for example, Li and Kuipers (2003) for an overview. In this work we use the relation from Wen and Yu (1966) which defines $f(\varepsilon)$ as a function of the void fraction ε:

$$f(\varepsilon) = \varepsilon^{-4.7}. \tag{19}$$

The weight force in Eq. (15) is simply $\boldsymbol{F}_g = m_{\mathrm{p}}\boldsymbol{g}$. It is important to note that the usual force correlations for, e.g., drag, Saffmann, and Magnus force are usually derived for single particles. There is a serious lack on understanding how these forces are modified depending on the local void fraction and cluster structures in dense particle flows which makes their application in such regimes questionable.

The sum of the torques acting on the particles in Eq. (15) is modeled as the sum of a fluid dynamic part and the torque from particle–particle and particle–wall collision as discussed in Section 2.3.3. For the fluid dynamic part of the torque due to viscous stresses we have:

$$T_{\mathrm{F}} = \frac{\rho_g}{2}\frac{d_{\mathrm{p}}^5}{2}C_{\mathrm{R}} \left|\boldsymbol{\Omega}\right| \boldsymbol{\Omega}, \tag{20}$$

where $\boldsymbol{\Omega}$ is a relative angular velocity between the particle and the fluid:

$$\boldsymbol{\Omega} = \frac{1}{2}(\nabla \times \boldsymbol{u}_g) - \omega \tag{21}$$

The torque coefficient C_{R} in Eq. (20) is given as:

$$C_{\mathrm{R}} = \begin{cases} \dfrac{12.9}{Re_{\mathrm{R}}^{0.5}} + \dfrac{128.4}{Re_{\mathrm{R}}}, & 32 < Re_{\mathrm{R}} < 1000 \\ \dfrac{64\pi}{Re_{\mathrm{R}}}, & Re_{\mathrm{R}} < 32 \end{cases} \tag{22}$$

with the rotational Reynolds number:

$$Re_{\mathrm{R}} = \frac{\rho_g d_{\mathrm{P}}^2 \left|\boldsymbol{\Omega}\right|}{\mu_g}. \tag{23}$$

The timestep of the particle movement has to follow the high frequency of the particle collision dynamics which leads typically to a very small timestep. Therefore it is usually sufficient to integrate the equations of motion, Eq. (14) with a simple integration scheme of first order in time. The numerical scheme can be summarized as:

$$x^{n+1} = x^n + (v^n + \dot{v}^n\, \Delta t)\Delta t, \qquad v^{n+1} = v^n + \dot{v}^n\, \Delta t,$$
$$\omega^{n+1} = \omega^n + \dot{\omega}^n\, \Delta t. \tag{24}$$

2.3.3. Spring damper collision model

To describe the collision dynamics in dense particulate flow it is nowadays common practice to use the soft-sphere approach. The soft-sphere approach usually models the contact forces between particles with springs, dash-pots, and a slider as shown in Fig. 1. The actual forces are calculated based on the (small) overlap between particles and allow a direct integration of the particle displacement based on the contact forces. Soft-sphere models not only allow the simulation of contact dynamics including multiple particle contacts, they also lead to a physically correct description of static particle systems, e.g., the bed height is preserved under the impact of gravity. A comparison of different contact force models can be found in Di Renzo and Di Maio (2004). Here we adopt the original linear spring/dash-pot model of Cundall and Strack (1979).

The contact forces in normal direction $\boldsymbol{F}_{nij}$ and in tangential direction $\boldsymbol{F}_{tij}$ acting on particle i due to the contact with particle
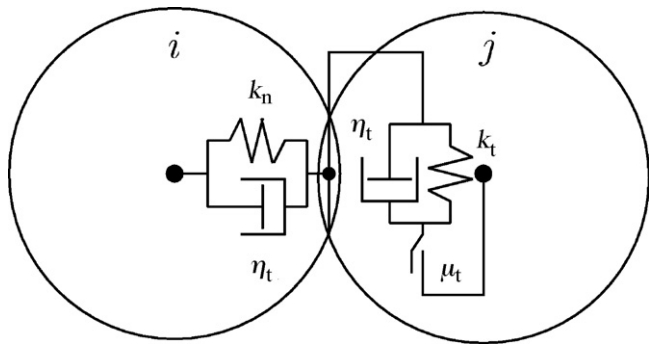
Fig. 1. Spring damper model used for collision modeling.

j as shown in Fig. 1 are modeled as:

$$\boldsymbol{F}_{nij} = (-k_n\delta_{nij} - \eta_n v_{rij}\boldsymbol{n}_{ij})\boldsymbol{n}_{ij}, \tag{25}$$

$$\boldsymbol{F}_{tij} = -k_t\delta_{tij} - \eta_t v_{sij}, \tag{26}$$

where k_n, k_t, η_n, η_t are the stiffness and damping coefficients in normal and tangential direction, v_{rij} is the relative velocity between particle i and j, and $\boldsymbol{n}_{ij}$ denotes the unit vector from the center of particle i to that of particle j.

In this study we have used values of $k_n = k_t = 800$ N/m taken from the work of Zhou et al. (2004a) for the stiffness coefficients. The damping coefficients $\eta_n = \eta_t = \eta$ are determined by the restitution coefficient $e = 0.95$ via $\eta = 2\gamma\sqrt{m_p k_n}$, with $\gamma = \alpha_s/\sqrt{1+\alpha_c^2}$ and $\alpha_c = (1/\pi)\ln(e)$ (Zhou et al., 2004a). The slip velocity at the contact point v_{sij} used in Eq. (26) can be expressed as:

$$v_{sij} = v_{rij} - (v_{rij} \cdot \boldsymbol{n}_{ij})\boldsymbol{n}_{ij} + (r_i\omega_i + r_j\omega_j) \times \boldsymbol{n}_{ij}, \tag{27}$$

where $\omega_{i|j}$ is the angular velocity of particle $i|j$ and $r_{i|j}$ its radius. If the relation:

$$\left|\boldsymbol{F}_{tij}\right| \geq \mu_f\left|\boldsymbol{F}_{nij}\right| \tag{28}$$

is satisfied, the particles slide in tangential direction and the tangential force is given by:

$$\boldsymbol{F}_{tij} = -\mu_f\left|\boldsymbol{F}_{nij}\right| t_{ij}, \tag{29}$$

with the friction coefficient $\mu_f = 0.3$ (Zhou et al., 2004a).

The net force and torque acting on a particle i due to particle–particle contacts are:

$$\boldsymbol{F}_{C,i} = \sum_j (\boldsymbol{F}_{nij} + \boldsymbol{F}_{tij}), \qquad \boldsymbol{T}_{C,i} = \sum_j (\boldsymbol{r}_i\boldsymbol{n}_{ij} \times \boldsymbol{F}_{tij}), \tag{30}$$

where the sum is over all particles j in contact with particle i.

2.4. Coupling and general solution method

The continuous gas phase equations are discretized in finite volume form and solved with a standard pressure based PISO solver for variable density flow using the open source software Open-FOAM (OpenFoam Programmers Guide, 2004). Advection terms are discretized with a second order upwind scheme whereas diffusive terms are calculated with standard second order central schemes.

Continuous gas phase and the particulate phase are alternatingly solved in time. The particle tracking was performed with a fixed timestep of 10^{-5} s which has been shown in numerical experiments to resolve the collision dominated particle movement in a smooth and continuous way. The (fixed) timestep used in the continuous gas phase solver has been chosen ten times the timestep used for integrating the particle in time. Stiff chemistry source
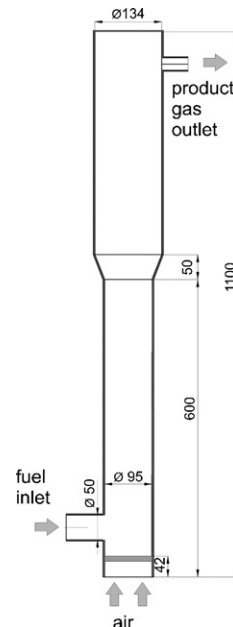

Fig. 2. Bubbling fluidized bed reactor at the Institute for Energy Engineering.

terms within the continuous and the particulate phase are integrated in time with the standard backward differencing formula (BDF) solver CVODE (Hindmarsh et al., 2005).

The coupling between the continuous gas phase and the discrete particles is done with a standard particle source in cell methodology which is the natural approach in a finite volume scheme. Mass, momentum and energy source terms are simply added to the discrete control volume where the particle resides in. When a particle has overlappings with more than one cell we split the volume for the calculation of the void fraction based on the partial volumes of the particle in the corresponding cells. For simplicity, for this splitting we assume the particle to be cubical with the same volume as the spherical particle.

3. Results and discussion

3.1. Experimental setup

The experimental data in this study were taken from a laboratory scale bubbling fluidized bed reactor at the Institute of Energy Engineering at Berlin University of Technology. Fig. 2 shows the reactor and its dimensions. The free board area and the bubbling bed zone have inner diameters of 134 and 95 mm, respectively. The walls of the reactor are heated on the outside with electrical heating coils. The reactor is operated at atmospheric pressure. The bed material consists of charcoal and pure wood and is fed in the lower part of the reactor with a feeding rate of 2 kg/h. Preheated air with a velocity of 0.25 m/s at a temperature of 400 °C enters the reactor from the bottom over the whole diameter of the reactor. The velocity of the air stream is slightly below the minimal fluidization velocity, i.e., fluidization of the bed and particle dynamics are strongly influenced by and dependent on pyrolysis, gasification, and gas phase reactions.

Six thermocouples inside the reactor at heights 5, 150, 325, 500, 700, and 900 mm above the air intake are monitoring the temperature inside the reactor. Product gases and tar components at the exit of the reactor are analyzed with a combination of gas chromatography and laser mass spectroscopy, see Neubauer and Behrendt (2007) for details.

Table 5
Time-averaged product gas concentrations at the outlet of the reactor for different wood feeding rates.

X	Simulation				Experiment	
	$\dot{m}_{wood} = 0.07$ kg/h	0.105 in kg/h	0.14 in kg/h	0.21 in kg/h	Min	Max
CO	0.15	0.19	0.21	0.25	0.13	0.21
CO_2	0.12	0.11	0.11	0.11	0.13	0.17
H_2	0.06	0.09	0.10	0.12	0.07	0.11

Fig. 3 shows experimental temperature data over time at different heights above the inlet in the reactor for a complete experiment. The reactor was started with a bed of pure charcoal and a pure heated nitrogen mass flow below the fluidization velocity to heat up the system. After the heating period of approximately 80 min the reactor was operated with heated air entering the reactor with a velocity of 0.25 m/s and a temperature of 400 °C. Between $t = 110$ min and $t = 130$ min the reactor runs at almost steady state conditions. We use the data from this time window to compare with numerical simulations.

3.2. Computational setup

The reactor shown in Fig. 2 has been discretized with a uniform grid spacing of 1 cm and a depth of 4 mm with one grid cell corresponding to the largest wood particles. Boundary conditions at the front and back of our quasi-3D domain have been set to slip conditions for the velocity and zero gradient for all scalar variables. For the two-dimensional simulations we have disabled the third coordinate within the particle tracking algorithm to ensure that particles move only within a plane. Inlet and boundary conditions are modeled to match the experimental setup as close as possible: heated air with a temperature of 670 K enters the reactor at the bottom with a velocity of $u = 0.25$ m/s, which is below the minimum fluidization velocity. That means fluidization under the investigated conditions is due to the acceleration of the fluid by exothermic chemical reactions and an increase of mole numbers within the gas phase by conversion of solid particles into gaseous compounds. Wood particles with an initial diameter of 4 mm and a density of 585 kg/m³ are injected through the fuel inlet with a temperature of 423 K. In the simulation the wood feeding rate from the experiment is transformed into a particle injection rate. Simulations have been performed for different wood feeding rates of $\dot{m}_{wood} = 0.07$, 0.105, 0.14, and 0.21 kg/h. The reference feeding rate of $\dot{m}_{wood} = 0.105$ kg/h corresponds exactly to the ratio of fuel to air supply in the experiment.

It is assumed that wood is completely dried at the fuel inlet and that the wood particles entering the reactor contain no water. However, the water content of the wood cannot be neglected and
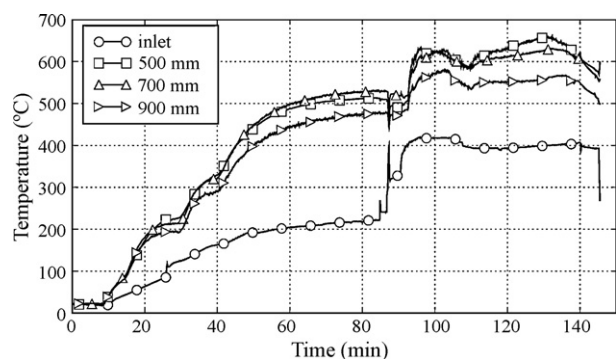
is modeled via a gaseous inlet stream of pure water vapor at a temperature of 423 K and a velocity of 0.079 m/s entering the reactor at the fuel inlet.

The walls of the reactor are modeled isothermal with a temperature of $T_W = 600$ K. It should be remarked that we have not validated the wall temperatures from the experiments and that a constant wall temperature of $T_W = 600$ K in the simulation is an approximation which can have a substantial impact on the results. We will investigate the influence of different temperature boundary conditions in a in press publication.
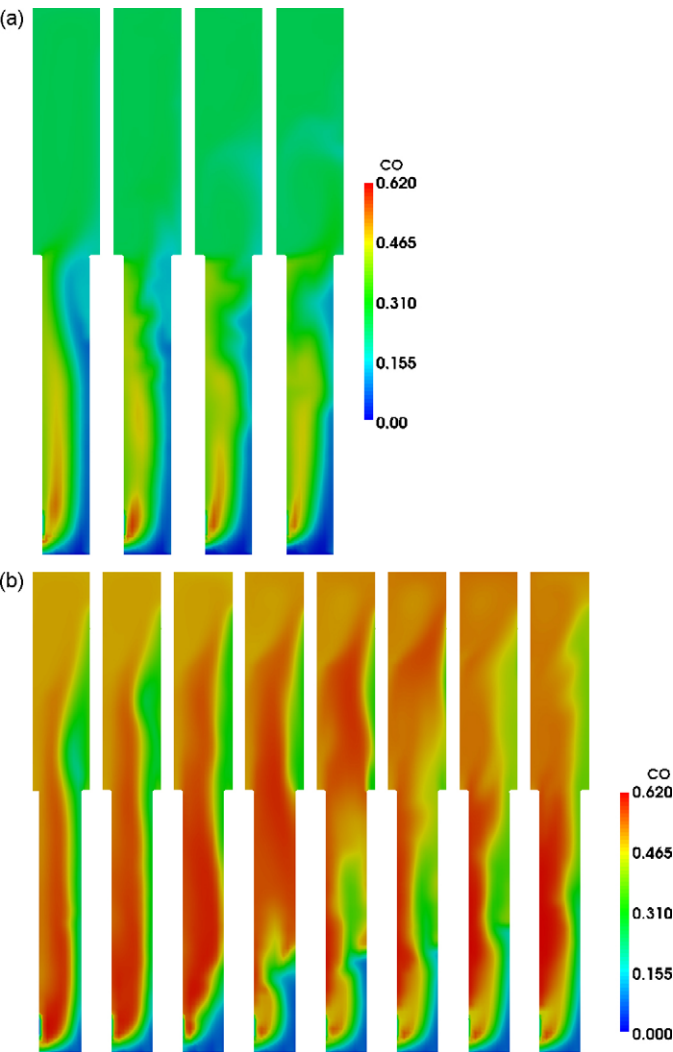
The reactor is filled at the beginning of the calculation with 4000 charcoal particles with diameter of 3 mm and a temperature of 1050 K. The number of charcoal particles has been chosen to match the bed height in the reactor with the experiment. The initial conditions correspond as close as possible to the conditions of the real reactor after heated up (time ~100 min in Fig. 3) with pure nitrogen.

3.3. Results

Fig. 4(a) and (b) shows snapshots of CO mass-fractions for wood feeding rates of $\dot{m}_{wood} = 0.105$ and 0.21 kg/h, respectively. The figures highlight the non-symmetric design of the reactor with the wood supply on the lower left side and the outlet at the upper right side of the reactor. CO production under the temperatures considered in this study is mainly due to the pyrolysis of wood into gaseous components which is an order of magnitude faster than CO production via gasification reactions of charcoal particles. These different timescales of CO production via pyrolysis and gasification lead to major CO production directly at the fuel inlet. In contrast, with the air inlet at the bottom of the reactor only charcoal particles are present leading to very low CO levels below the wood inlet. Fig. 4(a) and (b) shows also the qualitative influence of different wood feeding rates on the CO concentrations in the reactor. Although the qualitative pictures (main CO production via pyrolysis directly at the wood inlet) are the same for different wood feeding rates, we see increasing CO levels with increasing wood feeding rates—especially in the upper part of the reactor above the bed.

Fig. 5 shows product gas concentrations versus time at the outlet of the reactor for different feeding rates of wood. The figures clearly demonstrate the highly unsteady behavior of the fluidized bed. Higher wood feeding rates lead to higher CO and H_2 concentrations. With increasing wood feeding rates one can also observe higher frequencies and higher amplitudes of the concentration signals. This is due to an intensified fluidization at higher wood feeding rates. The higher wood feeding rates lead to more wood particles in the reactor which in turn results in higher production rates of gaseous components through heterogeneous gasification reactions. For small Mach-number flow this results immediately in a local acceleration within the gas phase and a boosted fluidization of the bed.
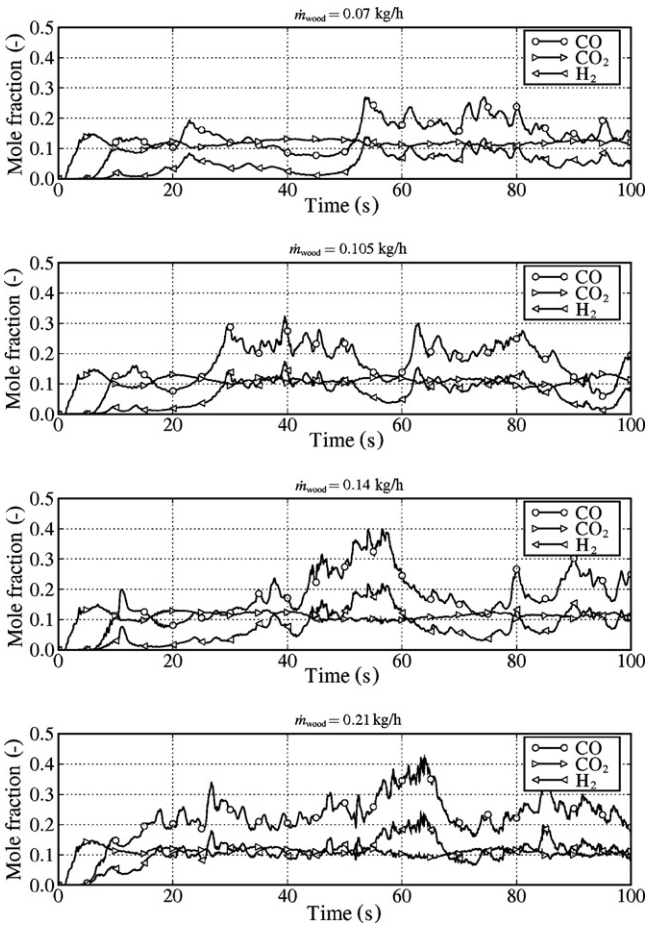
The intensified fluidization with increasing wood feeding rates can qualitatively be observed in the snapshots of the particle distributions shown in Fig. 6. The series of snapshots shows the typical fluidization behavior for wood feeding rates of $\dot{m}_{wood} = 0.105$ kg/h and $\dot{m}_{wood} = 0.21$ kg/h. In the case of a low feeding rate of $\dot{m}_{wood} = 0.105$ kg/h in Fig. 6(a) the bed is constantly fluidized

Fig. 3. Experimental temperature data over time for a complete run of the reactor at different heights.

(a)

(b)

Fig. 4. Snapshots of CO mass-fractions with the time increment between snapshots being 0.1 s for different wood feeding rates: (a) $\dot{m}_{wood} = 0.105$ kg/h and (b) $\dot{m}_{wood} = 0.21$ kg/h.

Fig. 5. Exhaust gas components versus time for different wood feeding rates $\dot{m}_{wood}$.

but gas bubbles are formed relatively seldom. For the high feeding rate of $\dot{m}_{wood} = 0.21$ kg/h (Fig. 6(b)) the character of the bed has changed into bubbling fluidization with eventual violent eruptions as in spout fluidized beds. This qualitative behavior has also been observed in the experiments and leads to increased amplitudes and frequencies as seen in Fig. 5.

Table 5 shows time-averaged product gas concentrations at the outlet of the reactor in comparison with experimental data, showing that the concentrations of typical gasification products (CO and H_2) increase with increasing wood feeding rates. In contrast, under partial oxidation conditions with relatively low temperatures of the bed material as considered here, the amount of CO_2 in the product gas is nearly independent of the wood feeding rate. This is due to the fact that CO_2 is a typical (combustion) product of the

gas phase reactions and the heterogeneous gasification reaction $C + O_2 \rightarrow CO_2$ and therefore mainly limited by the amount of available oxygen. However, as the mass flow rate of air has been kept constant, the amount of available oxygen was also constant. We note that an increased temperature of the charcoal particles would lead to an increased reaction rate of the heterogeneous reaction $C + CO_2 \rightarrow 2CO$ which has a direct impact on (i) the amount of CO and CO_2 in the product gas and (ii) the fluidization of the bed due to the creation/increase of gas phase mole numbers. Especially the second point highlights the subtle interaction of reaction kinetics and fluid mechanics/fluidization here. Table 5 also shows that the calculated product gas compositions for the reference wood feeding rate of $\dot{m}_{wood} = 0.105$ kg/h are within the variations seen in the experiments for the gasification products CO and H_2, whereas the CO_2 concentration is slightly under-predicted by the simulations.

Table 6 summarizes time-averaged temperature data at different heights in the reactor in comparison with experimental results, showing that the temperature is not very sensitive to variations in the wood feeding rate. This can be explained by the fact that the temperature within the reactor depends mainly on the exother-

Table 6
Time-averaged temperature data at different heights in the reactor for different wood feeding rates.

	Simulation				Experiment
	$\dot{m}_{wood} = 0.07$ kg/h	0.105 in kg/h	0.14 in kg/h	0.21 in kg/h	
$h = 500$ mm	858 K	883 K	850 K	895 K	905 K
$h = 700$ mm	756 K	793 K	777 K	882 K	805 K
$h = 900$ mm	757 K	792 K	776 K	827 K	796 K
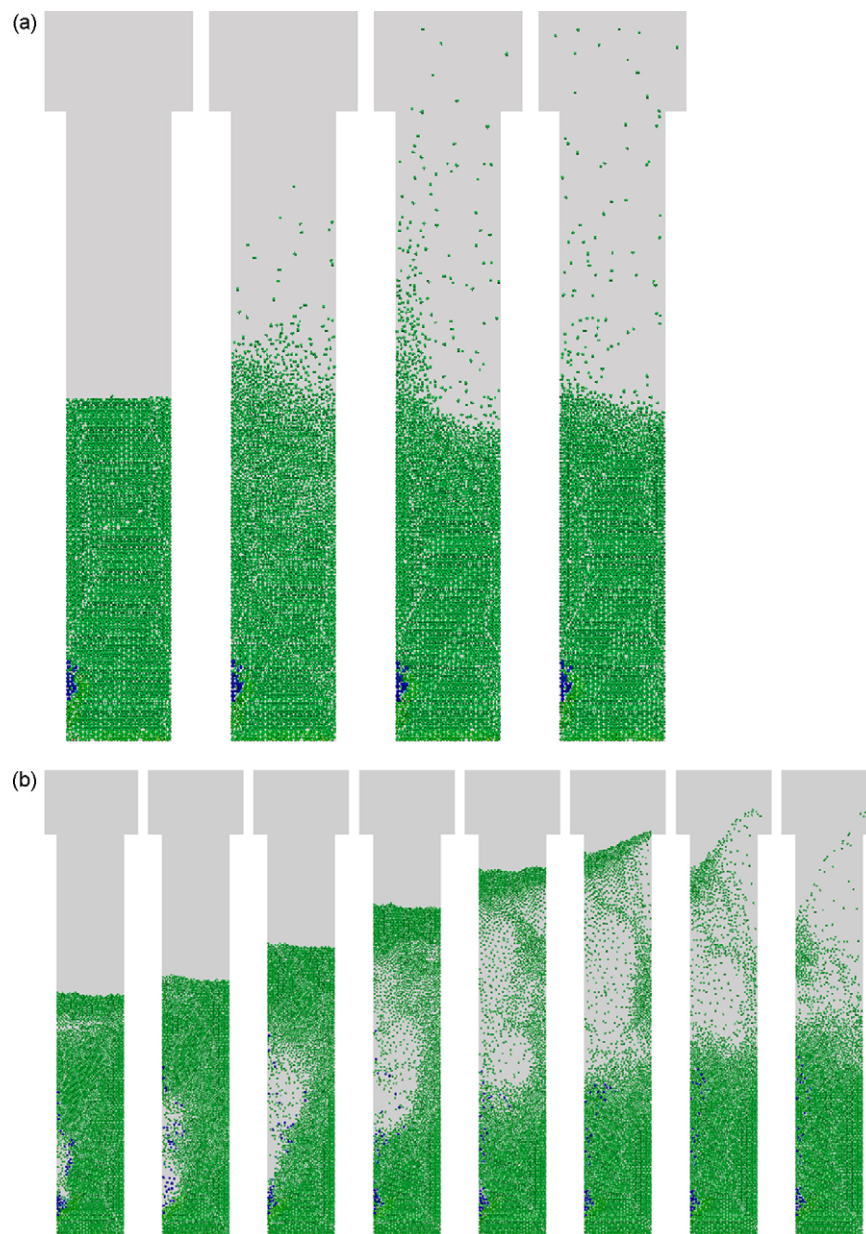
Fig. 6. Snapshots of particle distributions with the time increment between snapshots being 0.1 s and the particles colored by their diameter for different wood feeding rates: (a) $\dot{m}_{wood} = 0.105$ kg/h and (b) $\dot{m}_{wood} = 0.21$ kg/h.

mic oxidation reactions and therefore is limited by the amount of available oxygen. However, the overall temperature level of the experiment is reasonably well reproduced by the simulations. At heights 700 and 900 mm, i.e., in the free-board of the reactor in the experiments and the simulations, only the simulation with the highest wood feeding rate of $\dot{m}_{wood} = 0.21$ kg/h shows some change in temperature between the two heights. The difference of 100 K in the temperature level between 500 and 700 mm as seen in the experiments is well captured by the simulations. Unfortunately, we do not know the uncertainties in the experimental temperature data.

4. Conclusions

We have presented an Euler–Lagrange method for the simulation of wood gasification in a bubbling fluidized bed. The method uses a soft-sphere model for the collision dynamics in dense flu-

idized beds. We take into account detailed models for the pyrolysis and heterogeneous reactions on the individual particle level as well as a simple mechanism for the gas phase chemistry.

Simulation results for different feeding rates of wood show qualitatively a correct change in the fluidization behavior of the bed due to thermal expansion and devolatilization of wood and charcoal. The presented quantitative results for temperatures and product gas compositions agree reasonably well with the experimental data.

For this study we have used kinetic parameters and schemes from the literature without an attempt of tuning them to match the experimental data. A detailed investigation of different kinetic schemes and their influence on exhaust gas compositions, temperature, and the fluidization of the bed will be presented in a in press publication. The computing times for the presented calculations on a single core AMD Opteron running at 2.4 GHz clock speed are in the order of 10 s real-time per day. Even with massively parallel

computers it will be computationally very demanding to perform a (desirable) fully three-dimensional Euler–Lagrange simulation of chemically reacting gas–solid flow for a real size reactor and to produce statistically stationary results. A meaningful 2D model is therefore a viable tool for the simulation of larger systems and realistic operating times. A major challenge in further development of such 2D model will be an intelligent 2D/3D mapping of volumetric source terms due to the thermochemical conversion of solid wood as well as an adapted evaluation of the void fraction.

Due to the uncertainties and assumptions made in many parts of the modeling (e.g., 2D/3D particle dynamics, boundary conditions, wood composition, kinetic schemes, turbulence, etc.), the overall results of this study seem to be reasonable and promising for further improvements of the method.

Acknowledgments

References

Agrawal, K., Loezos, P. N., Syamlal, M., & Sundaresan, S. (2001). The role of meso-scale structures in rapid gas–solid flows. *Journal of Fluid Mechanics*, *445*, 151–185.

Biggs, M. J., & Agarwal, P. K. (1997). The CO/CO_2 product ratio for a porous char particle within an incipiently fluidized bed: A numerical study. *Chemical Engineering Science*, *52*(6), 941–952.

Cundall, P. A., & Strack, O. D. L. (1979). A discrete numerical model for granular assemblies. *Geotechnique*, *29*(1), 47–65.

De Souza-Santoz, M. L. (1989). Comprehensive modelling and simulation of fluidized bed boilers and gasifiers. *Fuel*, *68*(12), 1507–1521.

Deardoff, J. W. (1971). On the magnitude of the subgrid scale eddy coefficient. *Journal of Computational Physics*, *7*, 120–133.

Deen, N. G., Van Sint Annaland, M., Van der Hoef, M. A., & Kuipers, J. A. M. (2007). Review of discrete particle modeling of fluidized beds. *Chemical Engineering Science*, *62*, 28–44.

Di Blasi, C. (1996). Heat, momentum and mass transport through a shrinking biomass particle exposed to thermal radiation. *Chemical Engineering Science*, *51*, 1121–1132.

Di Renzo, A., & Di Maio, F. P. (2004). Comparison of contact-force models for the simulation of collisions in DEM-based granular flow codes. *Chemical Engineering Science*, *59*, 525–541.

Ding, J., & Gidaspow, D. (1990). A bubbling fluidization model using kinetic theory of granular flow. *AIChE Journal*, *36*(4), 523–538.

Dryer, F. L. (1972). *High temperature oxidation of CO and CH_4 in a turbulent flow reactor*. Unpublished doctoral dissertation, Princeton, NJ, USA: Princeton University.

Dryer, F. L., & Glassman, I. (1972). High-temperature oxidation of CO and CH_4. In *Proceedings of the 14th International Symposium on Combustion, Pittsburg, USA* (pp. 987–1003).

Gidaspow, D. (1994). *Multiphase flow and fluidization*. London: Academic Press.

Gronli, M. (1996). *A theoretical and experimental study of the thermal degradation of biomass*. Unpublished doctoral dissertation, Trondheim, Norway: The Norwegian University of Science and Technology.

Gungor, A. (2008). Two-dimensional biomass combustion modeling of CFB. *Fuel*, *87*, 1453–1468.

Hamel, S., & Krumm, W. (2001). Mathematical modeling and simulation of bubbling fluidized bed gasifiers. *Powder Technology*, *120*, 105–112.

Hindmarsh, A. C., Brown, P. N., Grant, K. E., Lee, S. L., Serban, R., Shumaker, D. E., et al. (2005). Sundials: Suite of nonlinear and differential/algebraic equation solvers. *ACM Transactions on Mathematical Software*, *31*(3), 363–396.

Hobbs, M. L., Radulovic, P. T., & Smoot, L. D. (1992). Modeling fixed-bed coal gasifiers. *AIChE Journal*, *38*(5), 681–702.

Jennen, T., Hiller, R., Köneke, D., & Weinspach, P.-M. (1999). Modeling of gasification of wood in a circulating fluidized bed. *Chemical Engineering & Technology*, *22*(10), 822–826.

Kaneko, Y., Shiojima, T., & Horio, M. (1999). DEM simulation of fluidized beds for gas-phase olefin polymerization. *Chemical Engineering Science*, *54*, 5809–5821.

Klein, R. (1999 January). Numerics in combustion. In L. Vervisch, & D. Veynante (Eds.), *Introduction to turbulent combustion*. Brussels, Belgium: von Karman Institute for Fluid Dynamics.

Klein, R., Botta, N., Schneider, T., Munz, C. D., Roller, S., Meister, A., et al. (2001). Asymptotic adaptive methods for multiscale problems in fluid mechanics. *Journal of Engineering Mathematics*, *39*, 261–343.

Kruggel-Emden, H., Wirtz, S., Simsek, E., & Scherer, V. (2006). Modeling of granular flow and combined heat transfer in hoppers by the discrete element method (DEM). *Journal of Pressure Vessel Technology*, *128*, 439–444.

Kuo, K. K. (1986). *Principles of combustion*. New York: John Wiley & Sons.

Lathouwers, D., & Bellan, J. (2001a). Modelling of dense gas–solid reactive mixtures applied to biomass pyrolysis in a fluidized bed. *International Journal of Multiphase Flow*, *27*, 2155–2187.

Lathouwers, D., & Bellan, J. (2001b). Yield optimization and scaling of fluidized beds for tar production from biomass. *Energy & Fuels*, *15*, 1247–1262.

Li, X. T., Grace, J. R., Lim, C. J., Watkinson, A. P., Chen, H. P., & Kim, J. R. (2004). Biomass gasification in a circulating fluidized bed. *Biomass and Bioenergy*, *26*(2), 171–193.

Li, J., & Kuipers, J. A. M. (2003). Gas–particle interactions in dense gas-fluidized beds. *Chemical Engineering Science*, *58*, 711–718.

Limtrakul, S., Boonsrirat, A., & Vatanatham, T. (2004). DEM modeling and simulation of a catalytic gas–solid fluidized bed reactor: A spouted bed as a case study. *Chemical Engineering Science*, *59*, 5225–5231.

Mitani, T., & Williams, F. A. (1980). Studies of cellular flames in hydrogen–oxygen–nitrogen mixtures. *Combustion and Flame*, *39*, 169–190.

Neubauer, Y., & Behrendt, F. (2007). Application of laser mass spectrometry for a fast and detailed online tar analysis in biomass gasification. In *Proceedings of the 15th European Biomass Conference & Exhibition, Berlin, May* (pp. 850–854).

O'Brien, T. J., Syamlal, M., & Guenther, C. (2003). Computational fluid dynamic simulations of chemically reactive fluidized bed processes. In *Proceedings of the 3rd International Conference on CFD in the Minerals and Process Industries, CSIRO, Melbourne, Australia, December* (pp. 469–474).

OpenFoam Programmers Guide (2004). *OpenFoam—The open source CFD toolbox—Programmer's guide* (1st Ed.). OpenCFD Limited, Web site: http://www.opencfd.co.uk/openfoam/.

Papadikis, K., Bridgwater, A. V., & Gu, S. (2008). CFD modelling of the fast pyrolysis of biomass in fluidised bed reactors. Part A. Eulerian computation of momentum transport in bubbling fluidised beds. *Chemical Engineering Science*, *63*, 4218–4227.

Papadikis, K., Gu, S., & Bridgwater, A. V. (2009a). CFD modelling of the fast pyrolysis of biomass in fluidised bed reactors: Modelling the impact of biomass shrinkage. *Chemical Engineering Journal*, *149*, 417–427.

Papadikis, K., Gu, S., & Bridgwater, A. V. (2009b). CFD modelling of the fast pyrolysis of biomass in fluidised bed reactors. Part B. Heat, momentum and mass transport in bubbling fluidised beds. *Chemical Engineering Science*, *64*, 1036–1045.

Radmanesh, R., Chaouki, J., & Guy, C. (2006). Biomass gasification in a bubbling fluidized bed reactor: Experiments and modeling. *AIChE Journal*, *52*(12), 4258–4272.

Rath, J., Wolfinger, M. G., Steiner, G., Krammer, G., Barontini, F., & Cozzani, V. (2003). Heat of wood pyrolysis. *Fuel*, *82*, 81–91.

Rong, D., & Horio, M. (1999). DEM simulation of char combustion in a fluidized bed. In *Proceedings of the 2nd International Conference on CFD in the Minerals and Process Industries, CSIRO, Melbourne, Australia, December* (pp. 65–70).

Ross, I. B., & Davidson, J. F. (1982). The combustion of carbon particles in a fluidized bed. *Chemical Engineering Research and Design*, *60a*, 108–114.

Smagorinsky, J. (1963). General circulation experiments with the primitive equations. I. The basic equations. *Monthly Weather Review*, *91*, 99–164.

Sommerfeld, M. (2000). *Theoretical and experimental modelling of particulate flows—overview and fundamentals, Part I and II*. Lecture Series 2000-06, April, von Karman Institute for Fluid Dynamics.

Tsuji, Y. (2000). Activities in discrete particle simulation in Japan. *Powder Technology*, *113*, 278–286.

Tsuji, Y., Kawaguchi, T., & Tanaka, T. (1993). Discrete particle simulation of two-dimensional fluidized bed. *Powder Technology*, *77*, 79–87.

Wen, C. Y., & Yu, Y. H. (1966). Mechanics of fluidization. *Chemical Engineering Symposium Series*, *62*, 100–111.

Wurzenberger, J. C., Wallner, S., Raupenstrauch, H., & Khinast, J. G. (2002). Thermal conversion of biomass: Comprehensive reactor and particle modeling. *AIChE Journal*, *48*(10), 2398–2411.

Zhong, W., Xiong, Y., Yuan, Z., & Zhang, M. (2006). DEM simulation of gas–solid flow behaviors in spout-fluid bed. *Chemical Engineering Science*, *61*, 1571–1584.

Zhou, H., Flamant, G., & Gauthier, D. (2004a). DEM–LES of coal combustion in a bubbling fluidized bed. Part I. Gas–particle turbulent flow structure. *Chemical Engineering Science*, *59*, 4193–4203.

Zhou, H., Flamant, G., & Gauthier, D. (2004b). DEM–LES simulation of coal combustion in a bubbling fluidized bed. Part II. Coal combustion at the particle level. *Chemical Engineering Science*, *59*, 4205–4215.